Check for updates

ADVANCED FUNCTIONAL MATERIALS
www.afm-journal.de

Realization of Complex-Shaped Magnetic Nanotubes with 3D Printing and Electrodeposition

Claudia Fernández-González, Pamela Morales-Fernández, Luke Alexander Turnbull, Claas Abert, Dieter Suess, Michael Foerster, Miguel Á. Niño, Pawel Nita, Anna Mandziak, Simone Finizio, Nuria Bagués, Eva Pereiro, Amalio Fernández-Pacheco, Lucas Pérez, Sandra Ruiz-Gómez,* and Claire Donnelly**

The expansion of nanomagnetism to the third dimension leads to phenomena such as curvature-induced magnetochirality and anisotropy, which can significantly influence the behavior of magnetic textures. One of the most promising systems is the magnetic nanotube – where intrinsic curvature effects are present. However, studies of magnetic nanotubes remain limited to straight systems, and little is known about the influence of 3D geometries. In this work, three dimensional (3D) complex-shaped nanotubes are fabricated by combining nanoprinting with the conformal deposition of magnetic films. Specifically, 3D conductive non-magnetic tungsten scaffolds are fabricated using focused electron beam induced deposition and subsequently coated with a nickel magnetic shell, resulting in complex-shaped magnetic nanotubes whose geometry can be controlled by tuning the electron-beam parameters and electrodeposition conditions. Performing X-ray microscopy revealed that nanotubes of various geometries host a vortex-like azimuthal state, and that the energy landscape of the magnetic configuration can be tailored geometrically. Specifically, the pinning of magnetic domain walls at curved vertices is observed experimentally and confirmed with micromagnetic simulations, offering geometrical control of magnetic configurations in nanotube architectures. This approach provides a new pathway to fabricate and study complex 3D core-shell magnetic structures, facilitating experimental investigations of their fundamental properties, key for the next-generation of spintronic devices.

1. Introduction

The natural extension of two dimensional (2D) films to curved geometries leads to new physical phenomena associated with geometric symmetry breaking. In magnetism, this introduction of curvature leads to the emergence of new properties such as curvature-induced anisotropy and magnetochirality.[1–3] One of the simplest structures encompassing this curvature is the nanotube, where symmetry breaking associated with the curved, tubular geometry has been predicted to result in asymmetric domain wall (DW) propagation and spin wave emission.[1,4–8] Additionally, the topology of the nanotube - where the magnetic material wraps around a core continuously, without the edges of two dimensional nanostrips - has been predicted to facilitate ultrafast DW propagation.[9–12] As a result, nanotubes represent a promising platform for the development of efficient, versatile, and multifunctional technologies.[13–18]

More generally, the extension to 3D nanogeometries offers a number of additional

C. Fernández-González, P. Morales-Fernández, L. A. Turnbull, S. Ruiz-Gómez, C. Donnelly
Max Planck Institute for Chemical Physics of Solids
01187 Dresden, Germany
E-mail: cfernandez@cells.es; Sandra.Gomez@cpfs.mpg.de; claire.donnelly@cpfs.mpg.de

C. Fernández-González, M. Foerster, M. Á. Niño, N. Bagués, E. Pereiro, S. Ruiz-Gómez
ALBA Synchrotron Light Source
CELLS
Cerdanyola del Valles, 08290 Barcelona, Spain

L. A. Turnbull, C. Donnelly
International Institute for Sustainability with Knotted Chiral Meta Matter (WPI-SKCM2)
Hiroshima University
Hiroshima 739-8526, Japan

C. Abert, D. Suess
Faculty of Physics
University of Vienna
1010 Vienna, Austria

C. Abert, D. Suess
Research Platform MMM Mathematics-Magnetism-Materials
University of Vienna
1010 Vienna, Austria

P. Nita
Faculty of Physics
Astronomy and Applied Computer Science
Jagiellonian University
30-348 Krakow, Poland

© 2025 The Author(s). Advanced Functional Materials published by Wiley-VCH GmbH. This is an open access article under the terms of the Creative Commons Attribution License, which permits use, distribution and reproduction in any medium, provided the original work is properly cited.

DOI: 10.1002/adfm.202515722

opportunities for magnetic systems - from the creation of chiral geometries leading to the formation of chiral and topological spin textures in achiral materials,[19–21] lateral curvature in nanowires allowing for the manipulation of the energy landscape of DWs,[22–24] as well as the prospect for high interconnectivity, a key aspect for the move to non-traditional computing architectures.[25]

However, so far such three dimensional (3D) phenomena have only been explored experimentally in the context of solid nanowires,[23,26–30] and investigations of magnetic nanotubes have been mainly limited to straight structures.[31–38] Indeed, the patterning of nanoscale 3D nanotube structures requires the combination of conformal deposition techniques with 3D nanoscaffolds. The combination of two-photon lithography and conformal deposition has led to the realization of 3D chiral and woodpile microstructures with atomic layer deposition,[39,40] and buckyball, spin ice and trefoil knot structures with electroless deposition,[41] albeit with tube diameters of hundreds of nanometres to micrometres. First realisations of nanotube geometries at spatial resolutions comparable to the characteristic lengths of nanomagnetism - i.e., on the order of tens of nanometres - has been achieved through the post-pyrolysis of two-photon lithography scaffolds,[42] as well as the combination of focused electron beam induced deposition with chemical vapor deposition (CVD) to synthesize curved 3D nanotubes suspended between prepatterned contact pads.[43] However, the fabrication of complex-shaped magnetic nanotubes featuring curvature, vorticity, helicity, or other intricate geometries remains challenging, and the influence of 3D geometries on the magnetic properties of nanotubes remains to be explored.

In this work, we present the experimental realisation and investigation of complex-shaped 3D nanotubes. To fabricate these structures, we combine Focused Electron Beam Induced Deposition (FEBID), with electrodeposition (ED) to achieve complex-shaped cylindrical nanotubes, including straight, helical, and zigzag nanotubes that encompass vertices. We gain insight into the magnetic configuration of these 3D nanotubes by performing X-ray photoelectron emission microscopy with X-ray magnetic circular dichroism (XMCD-PEEM), and reveal that they consistently exhibit an azimuthal magnetic configuration. By comparing the magnetic configuration of different geometries, we determine that designing the 3D structure of the nanotubes allows for the manipulation of the energy landscape of DWs. In particular, analogous to the pinning of transverse walls in curved magnetic nanowires, we observe that the vertices act as pinning sites, an effect that we confirm with finite element micromagnetic simulations. This new fabrication capability, combined with the insight into the influence of 3D geometries on the properties of nanotube structures, offers a route to explore the manipulation of magnetic textures in nanotubes of complex geometries.

2. Fabrication of 3D Nanotube Structures

To create 3D magnetic nanotube structures with arbitrary geometries, we combine 3D nanoprinting of a non-magnetic scaffold with the electrodeposition of magnetic materials. The fabrication process is presented in **Figure 1**. First, 3D non-magnetic nanostructures are directly printed on top of a conductive substrate by Focused Electron Beam Induced Deposition[44,45] (Figure 1a). Specifically, the 3D scaffolds are first designed with computer aided design software (CAD). Beam scanning patterns for the scanning electron microscope are then generated using the f3ast program[45,46] and used for the growth of the 3D scaffolds. In a second step, the sample is connected to an electrochemical cell to carry out the deposition of the magnetic shell on the conductive nanostructure (Figure 1b). After the electrodeposition, a core-shell structure of complex 3D geometry is obtained (see Figure 1c).

To prevent deposition of the magnetic layer on the wider conductive surface, and limit the growth to the 3D nanostructure, the substrate was prepared as follows. An insulating layer was deposited to passivate the surface of the substrate before the scaffold was grown. To ensure proper current flow through the FEBID W-C nanoscaffold (hereafter referred to as W), the insulating layer is selectively removed using Focused Ion Beam (FIB) etching prior to the nanoprinting process. The design of the sample for the case of silicon substrates is illustrated in Figure 1c, combining Au and AlO_x layers. In this way nanotubes of arbitrary geometry can be fabricated. We present the realisation of three different nanotube geometries in Figure 1d,e,f. For each of these geometries, SEM images of the non-magnetic W scaffolds are presented on the left. In the middle image, the nanostructure is shown following the deposition of the homogeneous Ni shell that covers the surface of the W to form the magnetic nanotubes. Finally, to visualize the relative dimensions of the core and shell components, the colored images presented on the right highlight the W core in pink and the magnetic shell in blue.

To verify the conformal growth of the Ni layer achieved by this multi-step fabrication method, Scanning Transmission Electron Microscopy - Energy Dispersive Spectroscopy (STEM-EDS) analysis was performed on cross sections of the nanostructures extracted with FIB (see **Figure 2**). Multiple lamellae were examined to assess the uniformity of Ni deposition in all directions, confirming the conformal coating of the magnetic shell. In the schematics shown in Figure 2a,b, the red planes indicate the orientation of the cross-sections extracted by FIB, which correspond to the High-Angle Annular Dark-Field (HAADF) images shown in Figure 2c and Figure 2e, respectively. Prior to lamella preparation, the samples were coated with a thin Au layer to prevent implantation of Ga ions during the FIB process. By

A. Mandziak
SOLARIS Synchrotron light Sources
30-392 Krakow, Poland
S. Finizio
Swiss Light Source
Paul Scherrer Institute
5232 Villigen PSI, Switzerland
A. Fernández-Pacheco
Institute of Applied Physics
TU Wien
Wiedner Hauptstr. 8-10/134, 1040 Vienna, Austria
L. Pérez
Dept. Física de Materiales
Universidad Complutense de Madrid
Plaza de las Ciencias 1, Madrid 28040, Spain
L. Pérez
Instituto Madrileño de Estudios Avanzados - IMDEA Nanociencia 9
Madrid 28049, Spain

© 2025 The Author(s). Advanced Functional Materials published by Wiley-VCH GmbH

16163028, 2026, 4, Downloaded from https://advanced.onlinelibrary.wiley.com/doi/10.1002/adfm.202515722 by Universidad Complutense De Madrid, Wiley Online Library on [16/02/2026]. See the Terms and Conditions (https://onlinelibrary.wiley.com/terms-and-conditions) on Wiley Online Library for rules of use; OA articles are governed by the applicable Creative Commons License

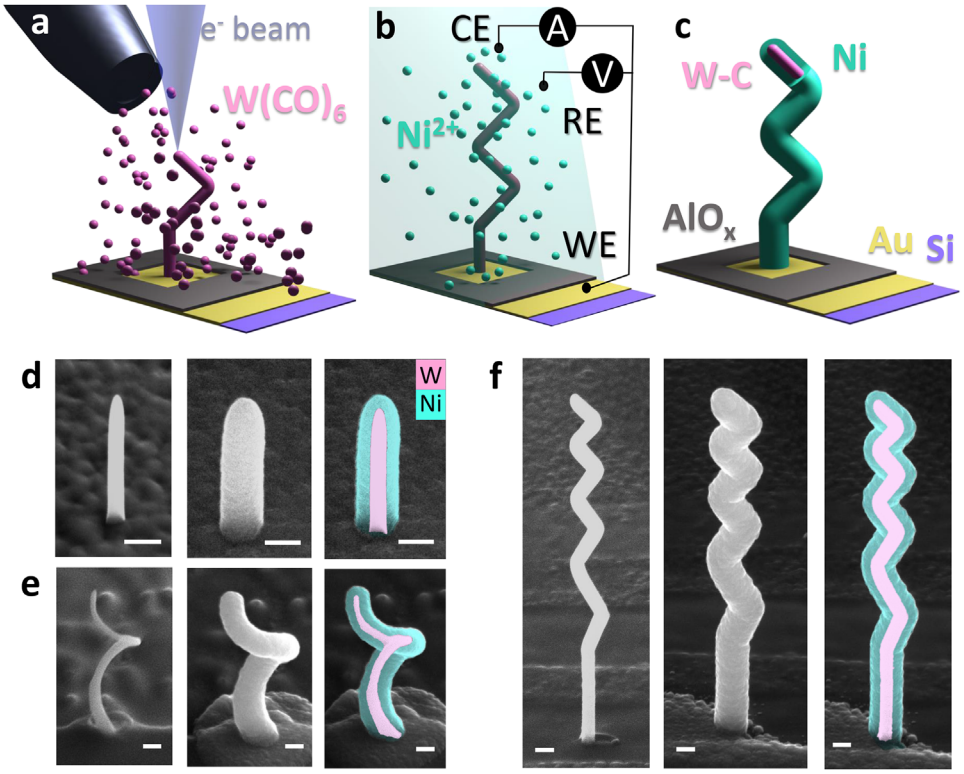

Figure 1. Fabrication of 3D nanotubes. a) Step 1: Direct patterning of the conductive W 3D nanostructure scaffolds by FEBID. b) Step 2: Electrodeposition of a magnetic nickel shell (CE: Counter Electrode; RE: Reference Electrode; WE: Working Electrode; A: current measurement; V: voltage application). c) A schematic of the resulting 3D nanotube structure is shown, where the non-magnetic tungsten core is given in pink, and the magnetic nickel shell given in blue. d,e,f) From left to right: scanning electron microscopy (SEM) images showing W nanostructures, W nanostructures covered with the Ni shell, and superimposed images to highlight the different layers of the nanostructure. Scale bar corresponds to 200 nm in all images.

comparing the HAADF images with the corresponding EDS elemental maps, the different materials within the structure can be clearly identified. The images reveal an amorphous W matrix uniformly coated by a polycrystalline Ni shell. The Ni layer consists of grains with varying crystallographic orientations, indicating the absence of a preferential growth direction. From left to right, the elemental maps display the total elemental distribution, followed by individual maps for W, Ni, C, and O. In panel (f), W was used as a support material during lamella preparation, which is the reason for its presence across the field of view. With these EDS maps, we can confirm that the W core is homogeneously covered by the Ni shell, with a smooth interface and no apparent oxidation. It should be noted that the intensities of the C and O maps were enhanced to improve visibility, and therefore the data for these elements are qualitative. When one considers normalized line profiles in Figure 2, negligible oxygen signal is observed at the W/Ni interface. The Ni signal is symmetric with respect to the W core in both profiles, further confirming the uniformity of the shell thickness. In (b), a slight increase in oxygen is observed on the outer surface of the Ni layer, which can be attributed to natural oxidation upon air exposure. However, this value may be overestimated as a result of the time elapsed between electrodeposition and lamella preparation (one year). Finally, we note that the Ni grain highlighted in white in panel (f) originated from an accidental second electrodeposition step and was not part of the original structure.

Having demonstrated the fabrication of 3D magnetic nanotube structures of a variety of geometries, we now turn our attention to the key geometric parameters of the nanotubes – specifically, the inner diameter and shell thickness – which play a crucial role in determining their magnetic configuration. Notably, by adjusting the inner diameter, it is possible to induce a transition from an axial to an azimuthal magnetic configuration.[47,48] In our approach, we are able to tune the inner diameter and thickness of the nanotubes by adjusting the electron beam current and voltage during the growth of the scaffold with FEBID.[49–51] We first consider the effect of increasing the beam current during FEBID by growing vertical nanowires with varying electron beam current. By comparing SEM images of W scaffold pillars grown with different currents (see **Figure 3**a, the complete set of SEM images is given in Figure S1, Supporting Information), the influence of the electron beam current on the morphology becomes evident. Pillars grown at low current values exhibit a narrower and constant diameter throughout the length of the wire. As the current increases, the pillar diameter expands, and a more conical shape begins to emerge, with a wider base, and a narrow tip at the end of the nanowire. Higher currents result in a larger diameter and a more pronounced pyramidal shape. This effect is particularly evident for current values around 2.8 nA and above, as can be seen in the Supporting Information.

In addition to the electron beam current, we also consider the influence of the electron beam voltage on the morphology of

© 2025 The Author(s). Advanced Functional Materials published by Wiley-VCH GmbH

16163028, 2026, 4, Downloaded from https://advanced.onlinelibrary.wiley.com/doi/10.1002/adfm.202515722 by Universidad Complutense De Madrid, Wiley Online Library on [16/02/2026]. See the Terms and Conditions (https://onlinelibrary.wiley.com/terms-and-conditions) on Wiley Online Library for rules of use; OA articles are governed by the applicable Creative Commons License

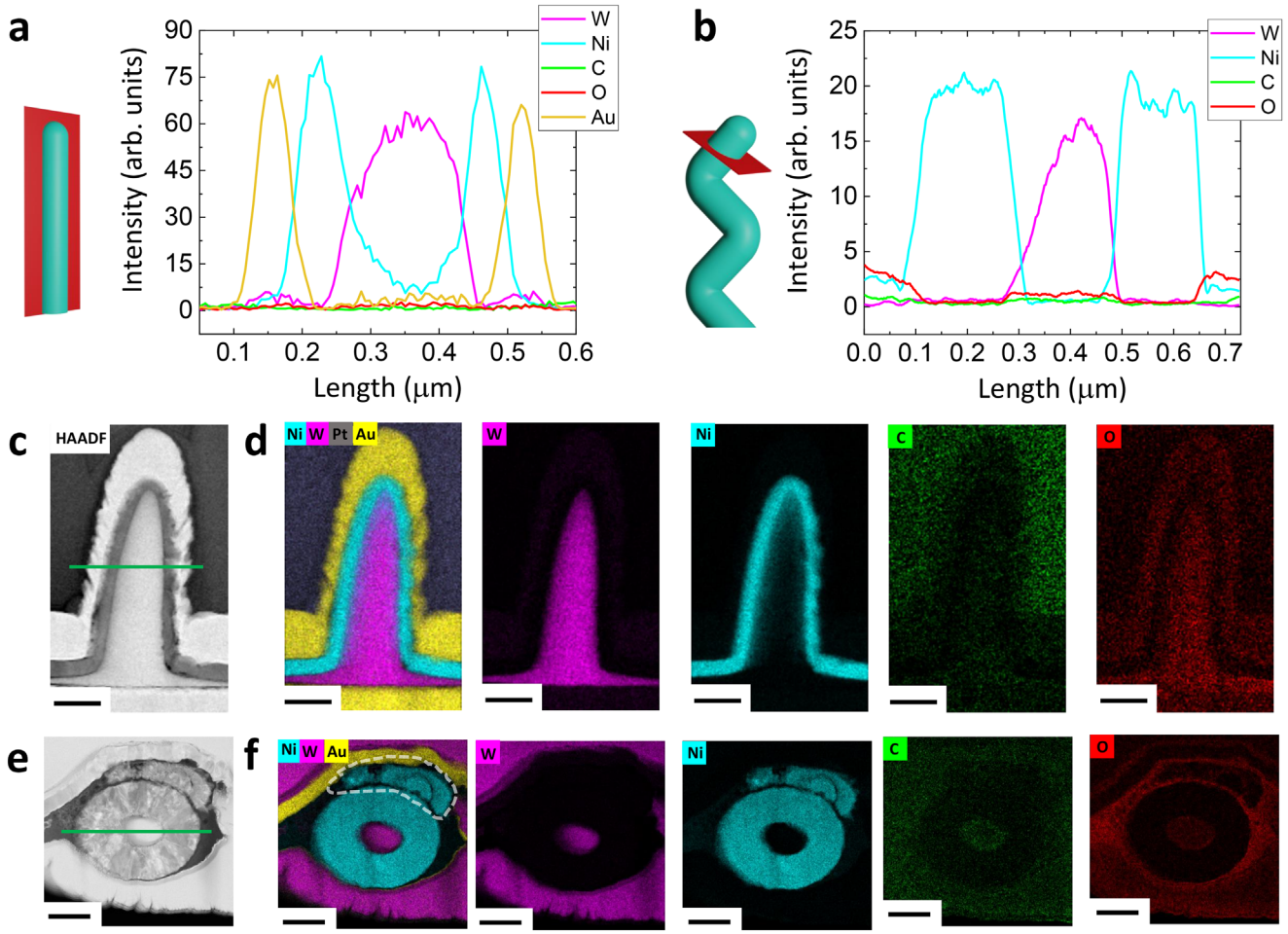

Figure 2. Morphology and compositional analysis of W/Ni nanotubes. a,b) Schematics showing the cross-sectional planes (red) analyzed in both straight and zigzag nanotubes, along with the corresponding compositional line profiles extracted from the regions marked by green lines in images (c) and (e), respectively. c,e) HAADF images and d,f) corresponding EDS maps illustrating the spatial distribution of W, Ni, C, and O. The white dashed line in (f) highlights a defect in the Ni shell originated from an accidental second electrodeposition step. The scale bar represents 200 nm in all images.

the pillars. Higher voltages result in thinner tubes with a uniform diameter, thus providing an improved cross-sectional spatial resolution, as seen in Figure S1 (Supporting Information). In Figure 3b, the values of the W scaffold diameters are plotted as a function of the electron beam current and voltage. It can be seen that narrower and more uniform nanowires can be achieved for lower currents and higher voltages, offering a route to tailor the inner diameter and 3D geometry of the nanotubes.[51]

Together with the inner diameter influencing the magnetic configuration, the thickness of the nanotube shell also impacts the magnetic state. Theoretical models predict that an increase in the nanotube thickness will promote the azimuthal magnetic configuration.[52] To gain control over the thickness of the film with high precision, the growth rate of the electrodeposition must be well-defined. While the inner diameter of the nanotube can be varied by changing the FEBID deposition parameters, this also leads to changes in composition (W and C content) in the inner scaffold, which can impact the conductivity,[53–55] and thus the growth rate of the magnetic shell. To determine the reliability of the growth process and deposition rate, we determine the deposition rate of Ni as a function of growth parameters of the W scaffold (V_{FEB} and I_{FEB}). When these are plotted in Figure 3c, we observe that as the V_{FEB} is increased, the growth rate of Ni increases from 29 ± 11 nms^{-1} with 6 kV to 37 ± 5 nms^{-1} with 30kV. The growth rate is also observed to increase with I_{FEB}, albeit slightly, indicating that the Ni deposition rate is predominantly influenced by the V_{FEB}. In both cases, larger V_{FEB} and I_{FEB} would result in the composition of the scaffold being affected,[56,57] making the W scaffold more conductive, reducing the ohmic drop in the electrode, increasing the cathodic density current and thus promoting higher growth rates. As the deposition rate of the Ni layer is mainly tuned by voltage of the FEBID process, and the inner diameter by the FEBID current, we therefore have an effective way to tune the geometric properties of the nanotubes.

3. Magnetic Configurations of 3D Nanotubes

Having demonstrated our fabrication technique to provide a robust route to realizing 3D magnetic nanotube architectures, we next consider their magnetic configuration, and the influence the

© 2025 The Author(s). Advanced Functional Materials published by Wiley-VCH GmbH

16163028, 2026, 4, Downloaded from https://advanced.onlinelibrary.wiley.com/doi/10.1002/adfm.202515722 by Universidad Complutense De Madrid, Wiley Online Library on [16/02/2026]. See the Terms and Conditions (https://onlinelibrary.wiley.com/terms-and-conditions) on Wiley Online Library for rules of use; OA articles are governed by the applicable Creative Commons License

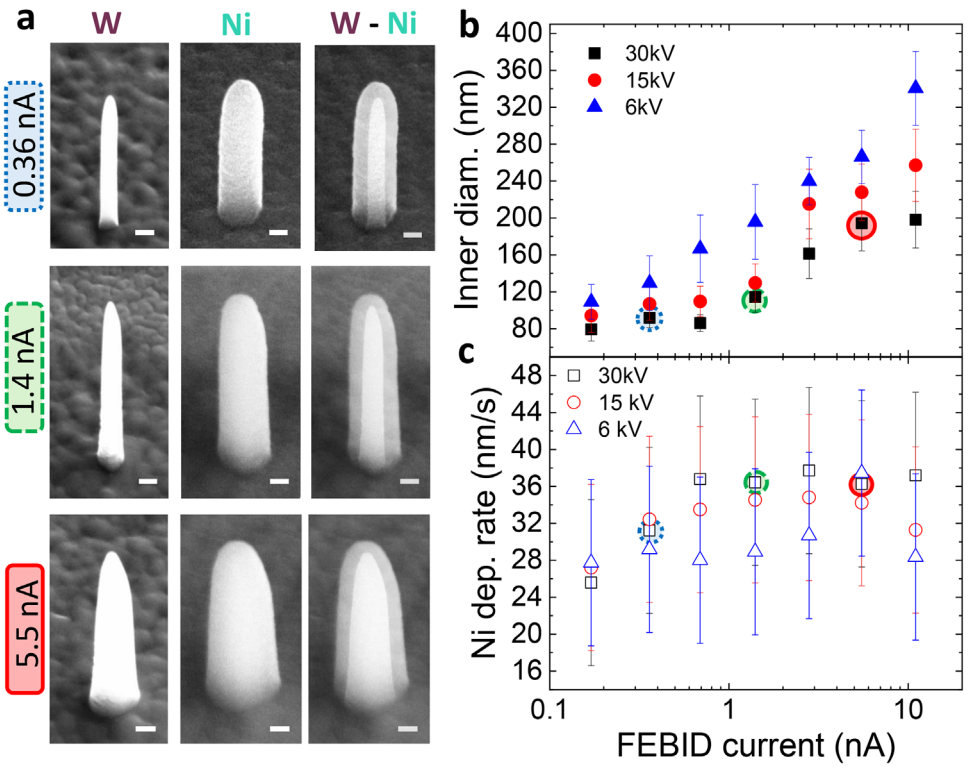

Figure 3. Relationship between deposition parameters and morphology of FEBID-ED straight nanotubes. a) SEM images of W single pillars, with the Ni shell, and superimposed W-Ni images presented. All pillars were grown via FEBID at $2e^{-7}$ mbar, using a beam voltage of 30 kV and a deposition time of 60 s. b,c) The dependence of the inner diameter of W pillars and the Ni electrodeposition rate on the e-beam current (I_{FEB}) and voltage settings (V_{FEB}) during the FEBID deposition of W scaffolds is illustrated. The scale bar corresponds to 100 nm in all images.

3D geometry can have. In general, there are two main types of domain configurations that can be present in magnetic nanotubes: the axial domains, in which the magnetisation aligns with the long axis, and azimuthal domains, in which the magnetization circulates around the tube. For both of these configurations, the presence of domain walls offers an opportunity to propagate information, or to excite spin waves in a system.[10,58] In 2D systems, or 3D nanowires, the geometry is well known to influence the domain wall energetics, and can be harnessed to realize, for example, controlled motion in devices.[23,59–62] A first insight into the influence of a curved nanotube on the domain wall energetics was gained with micromagnetic simulations[63] for the axial state. However, the lack of a suitable fabrication technique has limited experimental investigations of such effects in nanotubes until now.

Having established a protocol for the nanofabrication of magnetic nanotube architectures with arbitrary 3D geometries, we now have the ability to experimentally explore the influence of 3D geometries on the magnetic configuration. We perform magnetic microscopy to determine the magnetic configuration of the nanotubes, and gain insight into the magnetic properties of the deposited Ni shell. Specifically, we perform X-ray photoemission electron microscopy (PEEM) in the shadow geometry,[30,64–66] where X-rays illuminate the sample at grazing incidence to the substrate (see **Figure** 4a). In this configuration, the vertical nanotubes cast a shadow in the X-ray illumination of the substrate, which allows one to probe the spatially resolved absorption of the nanostructures, and thus probe the properties of the nanostructures.[67] We perform shadow PEEM with the X-ray energy tuned to the Ni L_3 edge, and measure images with positive and negative circular polarisation, exploiting X-ray magnetic circular dichroism (XMCD) to obtain projections of the component of the magnetisation parallel to the X-ray beam.

Dichroic projections reveal a strong XMCD signal, and a change in contrast in the direction perpendicular to the long axis of the tubes (see Figure 4b). This contrast is consistent with an azimuthal orientation of the magnetization, as it has been predicted theoretically for nanotubes of this range of diameter and thickness.[47] Indeed, when we perform finite element micromagnetic simulations of the magnetic state of a nanotube of similar geometry, we observe an azimuthal state, shown in Figure 4c. In this configuration, the magnetic moments lie tangential to the tube surface, and circulate around the long axis of the nanotube. In the case of the nanotubes shown here, due to the conformal growth of the magnetic shell, the azimuthal state is characterized by the presence of a magnetic vortex at the closed end of the tube (see Figure 4c, top). The strong XMCD signal, and the azimuthal state observed experimentally in the nanotubes further confirms the high quality, homogeneous shell of the nanotubes.

Having determined the presence of the azimuthal configuration in a straight nanotube, we next consider more complex geometries. As seen for the straight nanotube presented in Figure 4b, we observe the same azimuthal state in both the helical nanotube presented in Figure 4d, as well as for the "zigzag"

© 2025 The Author(s). Advanced Functional Materials published by Wiley-VCH GmbH

16163028, 2026, 4, Downloaded from https://advanced.onlinelibrary.wiley.com/doi/10.1002/adfm.202515722 by Universidad Complutense De Madrid, Wiley Online Library on [16/02/2026]. See the Terms and Conditions (https://onlinelibrary.wiley.com/terms-and-conditions) on Wiley Online Library for rules of use; OA articles are governed by the applicable Creative Commons License

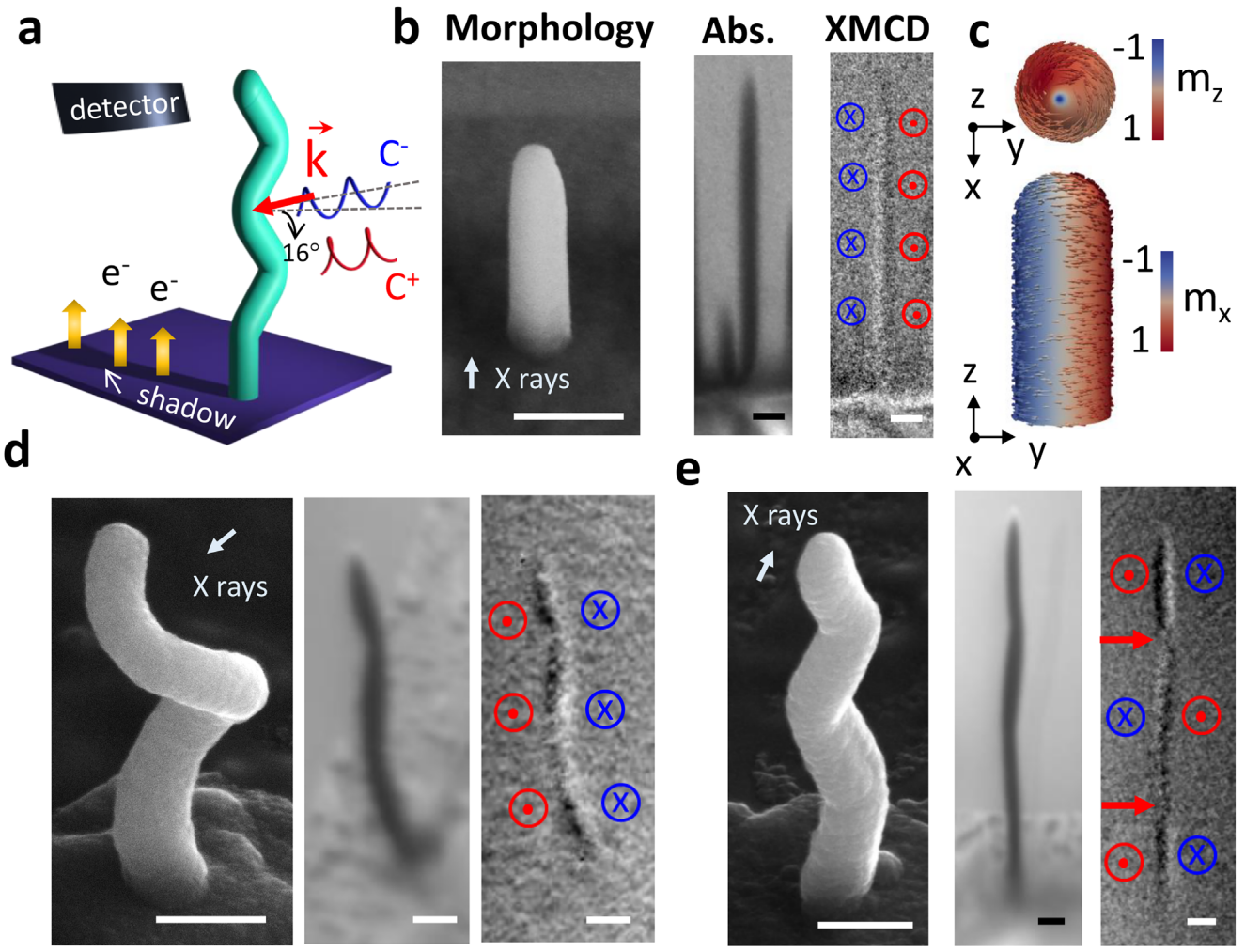

Figure 4. Observation of magnetic vortex state in complex-shape nanotubes by shadow-PEEM. a) Schematic of the XMCD shadow-PEEM measurements. b) SEM, absorption projection, and XMCD projection of a straight nanotube structure. The XMCD projection is consistent with the azimuthal configuration. c) Micromagnetic simulation of a straight nanotube in the remanence state, exhibiting the same azimuthal configuration. d,e) Corresponding SEM, absorption images and XMCD images of the "as grown" state for d) a helical nanotube, and e) a zigzag nanotube structure. d) the helical nanotube exhibits a single azimuthal domain configuration, whereas e) the zigzag structure exhibits multiple azimuthal domains, separated by DWs, that are indicated by the red arrows in the XMCD projection. The projection of the nanostructures is enlarged by a factor of 3.5x in the direction of the incident X-rays. Red and blue circles in XMCD images show the direction of the magnetization vector. Scale bar is 500 nm in all images.

nanotube with vertices in Figure 4e. Overall, considering that more than 40 nanotubes were characterized, the vast majority of them with Ni film thickness above 120 nm were observed to be in the azimuthal configuration, independent of the nanotube geometry, indicating that the azimuthal state is a well defined ground state of the system.

As well as being able to define particular domain configurations, obtaining control of magnetic defects such as DWs represents an important technological goal. DWs not only play an important role in mediating reversal processes (and providing control over the magnetic configuration), but offer additional prospects such as acting as information carriers[16,68] and as spin wave emitters.[6,69]

So far we have observed that in straight or helical nanotubes that have constant curvature or torsion, the nanotube always forms a single domain azimuthal state (see Figure 4b,d). However, in the zigzag structure, which incorporates vertices with local high curvature, a multi-domain state is commonly observed, with the presence of DWs that can be identified by an abrupt change in the azimuthal contrast with height. Examples of such DWs are highlighted by red arrows in Figure 4e, where they can be seen to form at what appear to be regular intervals within the structure.

4. Curvature-Induced Domain Wall Pinning

To determine whether DWs form at specific regions within the zigzag nanotube, the magnetic configuration was imaged after a series of different initialization procedures. In particular, during these initialization processes, an external magnetic field strong enough to saturate the magnetic configuration was applied either perpendicular or parallel to the long axis of the nanotube

© 2025 The Author(s). Advanced Functional Materials published by Wiley-VCH GmbH

16163028, 2026, 4, Downloaded from https://advanced.onlinelibrary.wiley.com/doi/10.1002/adfm.202515722 by Universidad Complutense De Madrid, Wiley Online Library on [16/02/2026]. See the Terms and Conditions (https://onlinelibrary.wiley.com/terms-and-conditions) on Wiley Online Library for rules of use; OA articles are governed by the applicable Creative Commons License

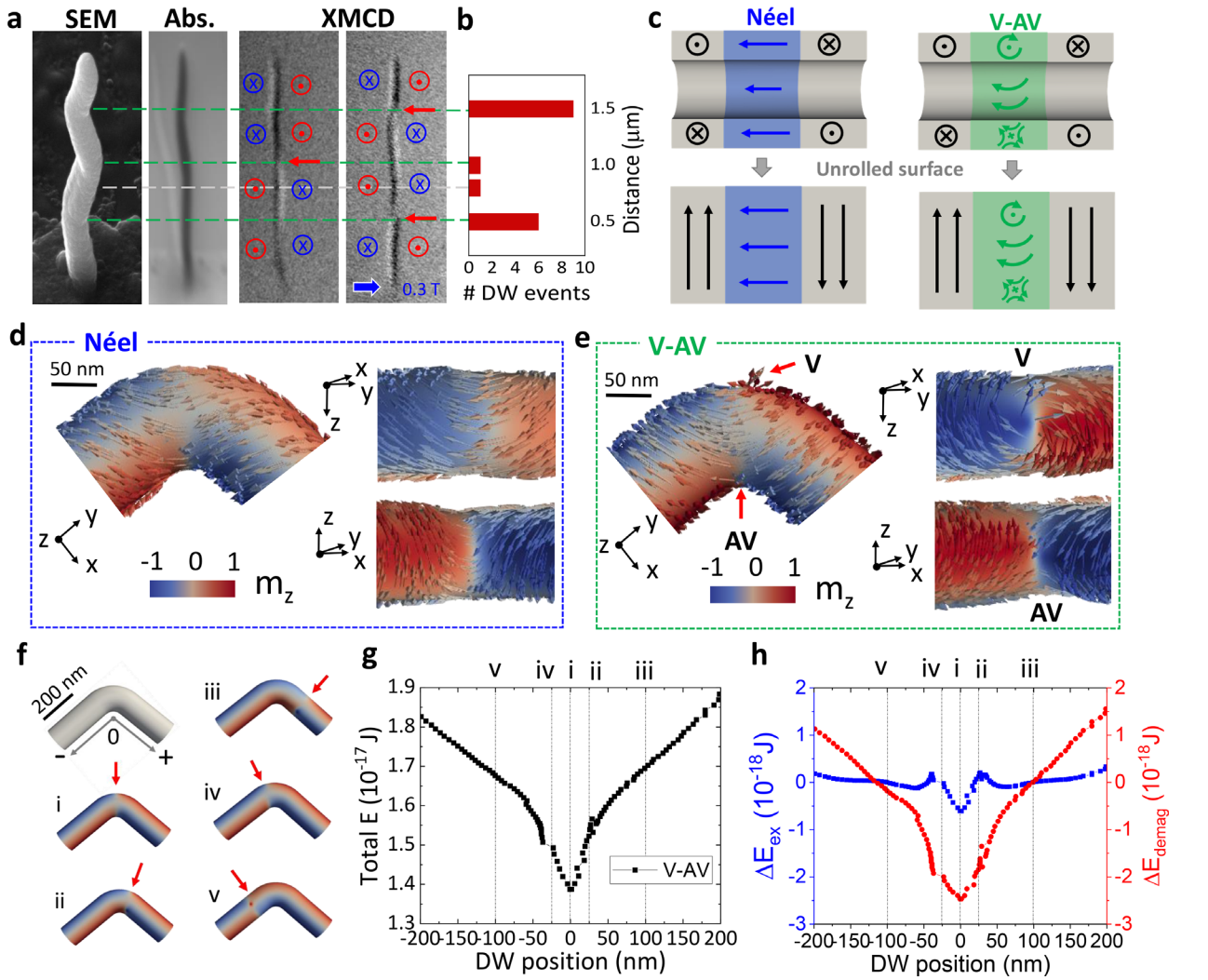

Figure 5. Pinning statistics in zigzag nanotubes. a) From left to right: SEM image of a zig-zag nanotube; shadow projection of the nanotube; XMCD images of the "as grown" state and after the application of external magnetic field of 0.3 T in the direction of the blue arrow). b) Histogram of DW pinning positions occurring in different regions of the nanotube. c) Schematics of the cross-section of a cylindrical nanotube with a Néel type and Vortex-Anti-Vortex (V-AV) type DWs. d,e) Micromagnetic simulations of Néel and V-AV DW at the vertex of the nanotube, respectively. f) Snapshots of the different positions of a V-AV DW through the zigzag nanotube, obtained by micromagnetic simulations under the application of a current density of 10^{12} Am^{-2}. g) Evolution of DW energy along the nanotube for V-AV DW. h) Exchange and magnetostatic contributions to the DW energy for the V-AV DW.

structure. XMCD projections of the nanotube structure in the "as-grown" state and after the application of 300 mT in the direction perpendicular to the long axis of the nanotube, are given in **Figure** 5a XMCD. To help with the interpretation of the XMCD projections, a SEM image and the shadow absorption projection of the nanotube structure are given. In the XMCD projection, in contrast to the straight and helical nanowires, domains of different azimuthal circulation are observed, between which DWs can be observed (highlighted by red arrows).

Indeed, multi-domain configurations with DWs are observed after all initialisations (see Figure S2, Supporting Information). When the positions of the DWs are plotted as a histogram next to the XMCD images in Figure 5b, 94% of the DWs consistently nucleate at heights corresponding to the vertices of the nanotube geometry (indicated by green dashed lines). Only one DW was observed near a vertex location (corresponding to the grey dashed line, Figure S2(iii), Supporting Information). These findings suggest the presence of a local energy minimum or pinning site for DWs at the vertices.

To determine the source of this pinning, we performed finite element micromagnetic simulations of a bent nanotube with a well-defined vertex using the finite element micromagnetic software package Magnum.pi.[70] First, we nucleated the DW at the vertex by defining two domains with opposite azimuthal orientations of the magnetization and relaxing the configuration.

During these simulations, it was possible to stabilise two types of DW at the vertex (see Figure 5c). The first was a Néel type DW where the magnetisation rotates about the radial direction of the nanotube, tilting from one domain to another. The second DW observed is a vortex-antivortex (V-AV) DW, characterized by a V-AV pair that forms within the DW, on opposite sides of the nanotube. The Néel wall was found to have a much higher energy

© 2025 The Author(s). Advanced Functional Materials published by Wiley-VCH GmbH

16163028, 2026, 4, Downloaded from https://advanced.onlinelibrary.wiley.com/doi/10.1002/adfm.202515722 by Universidad Complutense De Madrid, Wiley Online Library on [16/02/2026]. See the Terms and Conditions (https://onlinelibrary.wiley.com/terms-and-conditions) on Wiley Online Library for rules of use; OA articles are governed by the applicable Creative Commons License

16163028, 2026, 4, Downloaded from https://advanced.onlinelibrary.wiley.com/doi/10.1002/adfm.202515722 by Universidad Complutense De Madrid, Wiley Online Library on [16/02/2026]. See the Terms and Conditions (https://onlinelibrary.wiley.com/terms-and-conditions) on Wiley Online Library for rules of use; OA articles are governed by the applicable Creative Commons License

density than the V-AV wall (1.69 10^{-17} Jm^{-3} vs 1.39 10^{-17} Jm^{-3}), indicating that the V–AV configuration is more likely to be the stable DW state at the vertex of this structure.

To determine whether there is a pinning effect of the vertex, the total energy of the V-AV DW was calculated by micromagnetic simulations as a function of position along the nanotube. To propagate the DW along the tube, a current of 10^{12} Am^{-2} was applied between both ends of the tube, making use of the Zhang Li model to describe the spin torque.[71,72] This spin-transfer torque is expected to have a minimal effect on the domain wall structure, thereby providing a realistic estimation of the energy landscape as the domain wall propagates through the nanotube. For each position of the DW along the nanotube, the energy of the system was recorded in the presence of the current. The energy of the V-AV DW is plotted as a function of the DW position along the bent nanotube in Figure 5g. Five distinct positions are highlighted in the graph, corresponding to snapshots plotted in Figure 5f. These regions represent: i) the DW at the center of the vortex, ii, iv) the DW at the edge of the curved region, and iii, v) the DW at the straight part of the nanotube. The total energy of the V-AV wall decreases as the DW traverses the bent region (i), indicating the presence of a local energy minimum in the region of highest curvature, which is consistent with the preferential formation of DWs at the vertices observed experimentally.

To understand the origin of this local minimum, we considered the exchange and magnetostatic contributions separately. The local energy minimum at the vertex of the tube (i) is pronounced as both the exchange and magnetostatic energies reach their minimum values at this position (see Figure 5h). However, it can be seen that the decrease in magnetostatic energy is 4 times larger than for the exchange, indicating that this is a magnetostatics-dominated effect. These experimental and numerical results reveal that the vertex geometry - specifically the regions of high curvature - leads to effective pinning site for DWs in nanotubes with azimuthal domains, offering a route to the control of domain walls in nanotube geometries.

Moreover, the micromagnetic simulations reveal that these domain walls can propagate under the application of an electric current. This is particularly relevant for future experiments where domain wall motion can be induced by electrical currents, allowing for the evaluation and comparison of the contributions from spin-orbit torque and the Oersted field. In fact, the Oersted field generated by the current may offer an especially efficient mechanism to drive domain wall motion, particularly in nanotubes with azimuthal magnetization. Unlike axial systems—where large current densities are typically required to move domain walls—the azimuthal configuration enables more efficient propagation at lower current. This characteristic is highly advantageous for future experiments and potential device applications focused on current-driven DW dynamics in magnetic nanotube systems.

5. Conclusion and Outlook

In conclusion, we have achieved the experimental realisation of 3D magnetic nanotubes of arbitrary geometry through the growth of conductive 3D nanoscaffolds with focused electron beam induced deposition, and the subsequent electrodeposition of a magnetic shell. We demonstrate the fabrication of three different geometries of nanotubes - straight nanotubes, helical nanotubes, and zigzag nanotubes that incorporate vertices into the nanostructure. By performing a careful analysis of the influence of the electron beam parameters for the growth of the scaffold, we demonstrate control of the nanotube parameters, i.e., the inner diameter of the tube, and the thickness of the magnetic shell. We gain insight into the magnetic properties of the 3D nanotubes by performing X-ray magnetic microscopy. Using a combination of experiments and micromagnetic simulations, we not only show that magnetic nanotubes form vortex-like azimuthal magnetic domains, but also reveal that the domain walls — that separate domains of opposite azimuthal circulation — are pinned at the vertices, or areas of high curvature. While all nanotubes studied here exhibit the azimuthal state, reducing the diameter of the scaffold could enable the formation of axial domain configurations. This finding opens a pathway for controlling magnetic textures in nanotubes via the introduction of curved geometries. With the versatility of this 3D nanofabrication technique, the exploration of geometric effects is not limited to the introduction of curvature and torsion, but can be applied to a wide range of geometries encompassing, for example, interconnectivity, local geometric modulations, and non-trivial topologies.

The proposed technique offers not only the realization of complex 3D core-shell nanostructures but also the possibility to combine different materials such as superconducting W, magnetic Co, and Pt with electrodeposited magnetic shells. The combination of superconducting 3D scaffolds with ferromagnetic shells presents exciting opportunities for advancing the control and manipulation of both superconducting and magnetic properties in nanosystems.[73,74] The extension to interconnected nanostructures offers the possibility to design appropriate magnetic stray field templates for superconducting electronics[22] and proximity effects between the nanostructures, that can lead to long-range ordering and novel magnetic DW behavior.[75–77]

6. Experimental Section

FEBID patterning was performed using a Thermo Fisher Helios NanoLab 600 DualBeam microscope equipped with a commercial MultiChem Gas Injector System. The precursor gas used was $W(CO)_6$ and the growth was performed at $2e^{-7}$ mbar. Precursor gas was kept at room temperature during the growth. Prior to the FEBID patterning, insulating substrates were covered with a trilayer of Ti(5nm)/Au(70 nm)/Al(100 nm) via magnetron sputtering. The Al layer was "naturally" oxidated by exposing it to ambient conditions.

For the synthesis of the magnetic shell a PGSTAT204 potentiostat (Metrohm Autolab) was used. Deposition was performed in a three electrode cell using a Pt mesh as counter electrode and Ag/AgCl (NaCl 3 M) as reference electrode. Ni shell was deposited under the application of -1V (vs Ag/AgCl) from an electrolyte kept at room temperature composed of 0.76 M $NiSO_4$, 0.2 M $NiCl_2$ and 0.4 M H_3BO_3. The pH was adjusted to 2.5 adding H_2SO_4 10% vol.

The inner and outer diameter of the nanotubes was measured with Scanning Electron Microscopy (SEM). The electron beam parameters set for the image acquisition were 30 kV and 0.34 nA. The images were acquired with a substrate of the sample tilted at 52° to probe the full geometry of the nanostructures. The compositional and structural analysis of the nanotube was performed with scanning transmission electron microscopy (STEM) imaging combined with energy-dispersive X-ray spectroscopy (EDS) using a double-aberration-corrected Thermo Fisher Scientific Spectra 300 (S)TEM, operated at 300 kV. The microscope was

 © 2025 The Author(s). Advanced Functional Materials published by Wiley-VCH GmbH

equipped with a Super-X EDS detector, and the convergence angle used for the STEM-EDS analysis was 19.5 mrad. Vertical and transverse cross-section samples from the NWs were prepared by Ga ion milling at 30 and 5 kV using a focused ion beam (FIB) Helios 5 UX from Thermo Fisher Scientific for the STEM-EDS analysis.

Magnetic characterization of the nanotubes was performed with shadow XMCD-PEEM at the CIRCE[78] and DEMETER[79,80] beamlines from ALBA and SOLARIS synchrotron, respectively. Prior to the XMCD-PEEM measurements the sample was coated with an 15 nm thick layer of Au to increase conductivity and avoid charging effects. Absorption images were acquired for a photon energy corresponding to the Ni L_3 absorption edge for two opposite helicities. For the in situ application of magnetic fields of 80 mT in the out of plane direction, a dedicated out of plane sample holder was used.[81] Initialisations with 300 mT were performed ex situ using a permanent magnet.

Micromagnetic simulations were performed using the Magnum.pi code, applying a finite-element method. The mesh of the bent nanotube has the following dimensions: inner diameter of 60 nm, thickness of 30 nm, and a total length of 720 nm. The vertex has a radius of curvature of 110 nm and creates an angle of 100° between the two straight parts. These dimensions were chosen to match the experimentally investigated nanostructures. The mesh was discretized in tetrahedra, with a cell size of 4 nm. The parameters used for the simulation were $M_s = 4.85 \times 10^5$ Am^{-1}, $A_{ex} = 3.4 \times 10^{-12}$ Jm^{-1} and $\alpha = 0.1$. A current density of 10^{12} Am^{-2} was applied between the ends of the nanotube as a means to drive the DW through the nanotube via STT. The DW total energy (considering only exchange and dipolar contributions) was recorded along the conduit, neglecting the effect of the Oersted field generated by the current.

Supporting Information

Supporting Information is available from the Wiley Online Library or from the author.

Acknowledgements

This work received financial support from Spanish MCIN through Projects PID2020-117024GB-C43, PID2024-155385NB-C31 and PID2024-155385NA-C32, PID2021-122980OB-C54 from the Regional Government of Madrid under Project TEC-2024/TEC-380 Mag4TIC-CM and from the European Union's Horizon 2020 research and innovation programme under grant agreement No. 101007417, having benefited from the access provided by Paul Scherrer Institute (PSI) in Swiss Light Source (SLS) within the framework of the NFFA-Europe Pilot Transnational Access Activity, proposal [ID-408]. The authors acknowledged the CERIC-ERIC Consortium for the access to experimental facilities and financial support. This publication was partially developed under the provision of the Polish Ministry and Higher Education project "Support for research and development with the use of research infra-structure of the National Synchrotron Radiation Centre SOLARIS" under contract no 1/SOL/2021/2. C.F.G. and S.R.G. gratefully acknowledged the IEEE Magnetic Society Educational Seed Funding. S.R.G. also acknowledged funding from Marie Skłodowska-Curie Grant No. 101061612. L.A.T. acknowledged the support of the Alexander von Humboldt Foundation. REP-101061612-1. C.F.G, P.M.F., L.T., S.R.G. and C.D. acknowledged funding from the Max Planck Society Lise Meitner Excellence Program and funding from the European Research Council (ERC) under the ERC Starting Grant No. 3DNANOQUANT 101116043. N.B and S. R.G. acknowledged funding through Advanced Materials programme supported by MCIN with funding from the European Union NextGenerationEU (PRTR-C17.I1) and by the Generalitat de Catalunya. A.F.P. acknowledged funding by the European Community under the Horizon 2020 Program, contract number 101001290 (3DNANOMAG).

Conflict of Interest

The authors declare no conflict of interest.

Data Availability Statement

The data that support the findings of this study are available from the corresponding author upon reasonable request.

Keywords

3D nanomagnetism, electrodeposition, FEBID, nanotubes

Received: June 20, 2025
Revised: August 26, 2025
Published online: September 22, 2025

[1] R. Hertel, in *Spin*, volume 3 World Scientific, Singapore **2013**, p. 1340009.
[2] D. D. Sheka, O. V. Pylypovskyi, P. Landeros, Y. Gaididei, A. Kákay, D. Makarov, *Comm. Phys.* **2020**, *3*, 128.
[3] D. Makarov, O. M. Volkov, A. Kákay, O. V. Pylypovskyi, B. Budinská, O. V. Dobrovolskiy, *Adv. Mater.* **2022**, *34*, 2101758.
[4] M. Yan, C. Andreas, A. Kákay, F. García-Sánchez, R. Hertel, *Appl. Phys. Lett.* **2012**, *100*, 25.
[5] J. Otálora, J. López-López, P. Vargas, P. Landeros, *Appl. Phys. Lett.* **2012**, *100*, 7.
[6] L. Körber, R. Verba, J. A. Otálora, V. Kravchuk, J. Lindner, J. Fassbender, A. Kákay, *Phys. Rev. B* **2022**, *106*, 014405.
[7] R. Gallardo, P. Alvarado-Seguel, P. Landeros, *Phys. Rev. B* **2022**, *105*, 104435.
[8] M. M. Salazar-Cardona, L. Körber, H. Schultheiss, K. Lenz, A. Thomas, K. Nielsch, A. Kákay, J. A. Otálora, *Appl. Phys. Lett.* **2021**, *118*, 26.
[9] P. Landeros, Á. S. Nú nez, *J. Appl. Phys.* **2010**, *108*, 3.
[10] M. Yan, C. Andreas, A. Kákay, F. García-Sánchez, R. Hertel, *Appl. Phys. Lett.* **2011**, *99*, 12.
[11] K. Baumgaertl, F. Heimbach, S. Maendl, D. Rueffer, A. Fontcuberta i Morral, D. Grundler, *Appl. Phys. Lett.* **2016**, *108*, 13.
[12] R. Hertel, *J. Phys.: Condens. Matter* **2016**, *28*, 48.
[13] S. Ladak, A. Fernández-Pacheco, P. Fischer, *APL Mater.* **2022**, *10*, 12.
[14] A. Fernández-Pacheco, R. Streubel, O. Fruchart, R. Hertel, P. Fischer, R. P. Cowburn, *Nat. Commun.* **2017**, *8*, 1.
[15] G. Gubbiotti, A. Barman, S. Ladak, C. Bran, D. Grundler, M. Huth, H. Plank, G. Schmidt, S. van Dijken, R. Streubel, O. Dobrovoloskiy, V. Scagnoli, L. Heyderman, C. Donnelly, O. Hellwig, L. Fallarino, M. B. Jungfleisch, A. Farhan, N. Maccaferri, P. Vavassori, P. Fischer, R. Tomasello, G. Finocchio, R. Clérac, R. Sessoli, D. Makarov, D. D. Sheka, M. Krawczyk, R. Gallardo, P. Landeros, *J. Phys. Condens. Matter.* **2024**, *37*, 143502.
[16] K. Gu, Y. Guan, B. K. Hazra, H. Deniz, A. Migliorini, W. Zhang, S. S. Parkin, *Nat. Nanotechnol.* **2022**, *17*, 1065.
[17] J. Kim, A. J. Hong, S. M. Kim, K.-S. Shin, E. B. Song, Y. Hwang, F. Xiu, K. Galatsis, C. O. Chui, R. N. Candler, S. Choi, J.-T. Moon, K. L. Wang, *Nanotechnology* **2011**, *22*, 254006.
[18] A. V. Chumak, P. Kabos, M. Wu, C. Abert, C. Adelmann, A. Adeyeye, J. Åkerman, F. G. Aliev, A. Anane, A. Awad, et al., *IEEE Trans. Magn.* **2022**, *58*, 1.
[19] D. D. Sheka, V. P. Kravchuk, K. V. Yershov, Y. Gaididei, *Phys. Rev. B* **2015**, *92*, 054417.
[20] D. Sanz-Hernández, A. Hierro-Rodriguez, C. Donnelly, J. Pablo-Navarro, A. Sorrentino, E. Pereiro, C. Magén, S. McVitie, J. M. de Teresa, S. Ferrer, P. Fischer, A. Fernández-Pacheco, *ACS Nano* **2020**, *14*, 8084.
[21] C. Donnelly, A. Hierro-Rodríguez, C. Abert, K. Witte, L. Skoric, D. Sanz-Hernández, S. Finizio, F. Meng, S. McVitie, J. Raabe, D. Suess,

© 2025 The Author(s). Advanced Functional Materials published by Wiley-VCH GmbH

16163028, 2026, 4, Downloaded from https://advanced.onlinelibrary.wiley.com/doi/10.1002/adfm.202515722 by Universidad Complutense De Madrid, Wiley Online Library on [16/02/2026]. See the Terms and Conditions (https://onlinelibrary.wiley.com/terms-and-conditions) on Wiley Online Library for rules of use; OA articles are governed by the applicable Creative Commons License

R. Cowburn, A. Fernández-Pacheco, *Nat. Nanotechnol.* **2022**, *17*, 136.
[22] O. M. Volkov, A. Kákay, F. Kronast, I. Mönch, M.-A. Mawass, J. Fassbender, D. Makarov, *Phys. Rev. Lett.* **2019**, *123*, 077201.
[23] S. Ruiz-Gómez, C. Abert, P. Morales-Fernández, C. Fernández-González, S. Koraltan, L. Danesi, D. Suess, M. Varela, G. Sánchez-Santolino, N. Bagués, M. Foerster, M. Niño, A. Mandziak, D. Wilgocka-Slezak, P. Nita, M. Koenig, S. Seifert, A. Hierro-Rodriguez, A. Fernández-Pacheco, C. Donnelly, *Nat. Commun.* **2025**, *16*, 7422.
[24] A. M. Farinha, S.-H. Yang, J. Yoon, B. Pal, S. S. Parkin, *Nature* **2025**, *639*, 67.
[25] E. C. Burks, D. A. Gilbert, P. D. Murray, C. Flores, T. E. Felter, S. Charnvanichborikarn, S. O. Kucheyev, J. D. Colvin, G. Yin, K. Liu, *Nano Lett.* **2021**, *21*, 716
[26] M. Schöbitz, A. De Riz, S. Martin, S. Bochmann, C. Thirion, J. Vogel, M. Foerster, L. Aballe, T. Menteş, A. Locatelli, A. Locatelli, F. Genuzio, S. Le-Denmat, L. Cagnon, J. C. Toussaint, D. Gusakova, J. Bachmann, O. Fruchart, *Phys. Rev. Lett.* **2019**, *123*, 217201.
[27] M. Schöbitz, S. Finizio, A. De Riz, J. Hurst, C. Thirion, D. Gusakova, J.-C. Toussaint, J. Bachmann, J. Raabe, O. Fruchart, *Appl. Phys. Lett.* **2021**, *118*, 17.
[28] L. Alvaro-Gómez, A. Masseboeuf, N. Mille, S. Ruiz-Gómez, J. Toussaint, R. Belkhou, M. Foerster, E. Pereiro, L. Aballe, C. Thirion, D. Gusakova, O. Fruchart, L. Pérez, *arXiv preprint arXiv:2405.00652* **2024**.
[29] E. Berganza, M. Jaafar, C. Bran, J. A. Fernández-Roldán, O. Chubykalo-Fesenko, M. Vázquez, A. Asenjo, *Sci. Rep.* **2017**, *7*, 11576.
[30] S. Ruiz-Gómez, M. Foerster, L. Aballe, M. P. Proenca, I. Lucas, J. L. Prieto, A. Mascaraque, J. de la Figuera, A. Quesada, L. Pérez, *Sci. Rep.* **2018**, *8*, 16695.
[31] M. C. Giordano, K. Baumgaertl, S. Escobar Steinvall, J. Gay, M. Vuichard, A. Fontcuberta i Morral, D. Grundler, *ACS Appl. Mater. Interfaces* **2020**, *12*, 40443.
[32] M. C. Giordano, S. E. Steinvall, S. Watanabe, A. F. i Morral, D. Grundler, *Nanoscale* **2021**, *13*, 13451.
[33] M. Staňo, S. Schaefer, A. Wartelle, M. Rioult, R. Belkhou, A. Sala, T. O. Menteş, A. Locatelli, L. Cagnon, B. Trapp, S. Bochmann, S. Y. Martin, E. Gautier, J.-C. Toussaint, W. Ensinger, O. Fruchart, *SciPost Phys.* **2018**, *5*, 038.
[34] L. Körber, M. Zimmermann, S. Wintz, S. Finizio, M. Weigand, J. Raabe, J. A. Otálora, H. Schultheiss, E. Josten, J. Lindner, et al., *arXiv preprint arXiv:2009.02238* **2020**.
[35] M. C. Giordano, M. Hamdi, A. Mucchietto, D. Grundler, *Phys. Rev. Mater.* **2023**, *7*, 024405.
[36] F. Muench, S. Schaefer, M. Méndez, J. A. Fernández-Roldán, A. S. González-García, V. Vega, U. Kunz, W. Ensinger, J. García, V. M. Prida, *J. Mater. Chem. C.* **2023**, *11*, 9271.
[37] D. Tiwari, M. C. Scheuerlein, M. Jaber, E. Gautier, L. Vila, J.-P. Attané, M. Schöbitz, A. Masseboeuf, T. Hellmann, J. P. Hofmann, W. Ensinger, O. Fruchart, *J. Magn. Magn. Mater.* **2023**, *575*, 170715.
[38] M. Wyss, A. Mehlin, B. Gross, A. Buchter, A. Farhan, M. Buzzi, A. Kleibert, G. Tütüncüoglu, F. Heimbach, A. Fontcuberta i Morral, et al., *Phys. Rev. B* **2017**, *96*, 024423.
[39] H. Guo, A. J. M. Deenen, M. Xu, M. Hamdi, D. Grundler, **2023**, *35*, 2303292.
[40] M. Xu, A. J. M. Deenen, H. Guo, D. Grundler, Room temperature realization of artificial chiral magnets with reprogrammable magnon nonreciprocity at zero field, http://arxiv.org/abs/2404.19153, Version: 2.
[41] P. Pip, C. Donnelly, M. Döbeli, C. Gunderson, L. J. Heyderman, L. Philippe, *Small* **2020**, *16*, 2004099.
[42] S. Gliga, G. Seniutinas, A. Weber, C. David *26*, 100.
[43] F. Porrati, S. Barth, G. C. Gazzadi, S. Frabboni, O. M. Volkov, D. Makarov, M. Huth, *ACS Nano* **2023**, *17*, 4704.
[44] I. Utke, S. Moshkalev, P. Russell, *Nanofabrication using focused ion and electron beams: principles and applications*, Oxford University Press, Oxford **2012**.
[45] L. Skoric, D. Sanz-Hernández, F. Meng, C. Donnelly, S. Merino-Aceituno, A. Fernández-Pacheco, *Nano Lett.* **2019**, *20*, 184.
[46] L. Skoric, Algorithm to perform layer-by-layer nanoscale 3d printing by focused electron beam induced deposition, https://www.tuwien.at/phy/iap/physics-of-three-dimensional-nanomaterials/software/f3ast.
[47] P. Landeros, O. Suarez, A. Cuchillo, P. Vargas, *Phys. Rev. B.* **2009**, *79*, 024404.
[48] C. Sun, V. L. Pokrovsky, *J. Magn. Magn. Mater.* **2014**, *355*, 121.
[49] W. Van Dorp, C. W. Hagen, *J. Appl. Phys.* **2008**, *104*, 8.
[50] H. Plank, R. Winkler, C. H. Schwalb, J. Hütner, J. D. Fowlkes, P. D. Rack, I. Utke, M. Huth, *Micromachines* **2019**, *11*, 48.
[51] R. Winkler, B. B. Lewis, J. D. Fowlkes, P. D. Rack, H. Plank, *ACS Appl. Nano Mater.* **2018**, *1*, 1014.
[52] J. Hurst, A. De Riz, M. Staňo, J.-C. Toussaint, O. Fruchart, D. Gusakova, *Phys. Rev. B* **2021**, *103*, 024434.
[53] P. M. Weirich, M. Winhold, C. H. Schwalb, M. Huth, *Beilstein J. Nanotechnol.* **2013**, *4*, 919.
[54] V. Reisecker, R. Winkler, H. Plank, *Adv. Funct. Mater.* **2024**, *34*, 2407567.
[55] M. Huth, D. Klingenberger, C. Grimm, F. Porrati, R. Sachser, *New J. Phys.* **2009**, *11*, 033032.
[56] R. Córdoba, N. Sharma, S. Kölling, P. M. Koenraad, B. Koopmans, *Nanotechnol.* **2016**, *27*, 355301.
[57] R. Córdoba, J. Sesé, J. De Teresa, M. R. Ibarra, *Microelectron. Eng.* **2010**, *87*, 1550.
[58] J. A. Otálora, M. Yan, H. Schultheiss, R. Hertel, A. Kákay, *Phy. Rev. B* **2017**, *95*, 184415.
[59] D. D. Sheka, *Appl. Phys. Lett.* **2021**, *118*, 23.
[60] D. D. Sheka, O. V. Pylypovskyi, O. M. Volkov, K. V. Yershov, V. P. Kravchuk, D. Makarov, *Small* **2022**, *18*, 2105219.
[61] K. V. Yershov, V. P. Kravchuk, D. D. Sheka, Y. Gaididei, *Phy. Rev. B* **2015**, *92*, 104412.
[62] E. Berganza, F. Tejo, G. H. Bittencourt, V. L. Carvalho-Santos, O. Chubykalo-Fesenko, A. Asenjo, *Small* **2025**, *21*, 2407084.
[63] L. Skoric, C. Donnelly, C. Abert, A. Hierro-Rodriguez, D. Suess, A. Fernández-Pacheco, *Appl. Phys. Lett.* **2021**, *118*, 24.
[64] S. Da Col, S. Jamet, N. Rougemaille, A. Locatelli, T. O. Mentes, B. S. Burgos, R. Afid, M. Darques, L. Cagnon, J.-C. Toussaint, et al., *Phys. Rev. B* **2014**, *89*, 180405.
[65] R. Streubel, D. Makarov, F. Kronast, V. Kravchuk, M. Albrecht, O. G. Schmidt, *Phys. Rev. B* **2012**, *85*, 174429.
[66] R. Streubel, L. Han, F. Kronast, A. A. Ünal, O. G. Schmidt, D. Makarov, *Nano Letters* **2014**, *14*, 3981.
[67] A. Wartelle, J. Pablo-Navarro, M. Staňo, S. Bochmann, S. Pairis, M. Rioult, C. Thirion, R. Belkhou, J. M. de Teresa, C. Magén, O. Fruchart, *Nanotechnology* **2017**, *29*, 045704.
[68] S. S. Parkin, M. Hayashi, L. Thomas, *Science* **2008**, *320*, 190.
[69] R. B. Holländer, C. Müller, J. Schmalz, M. Gerken, J. McCord, *Sci. Rep.* **2018**, *8*, 13871.
[70] C. Abert, L. Exl, F. Bruckner, A. Drews, D. Suess, *J. Magn. Magn. Mater.* **2013**, *345*, 29.
[71] S. Zhang, Z. Li, *Phys. Rev. Lett.* **2004**, *93*, 127204.
[72] C. Abert, *Eur. Phys. J. B* **2019**, *92*, 1.
[73] E. Zhakina, L. A. Turnbull, W. Xu, M. König, P. Simon, W. Carrillo-Cabrera, A. Fernández-Pacheco, U. Vool, D. Suess, C. Abert, V. M. Fomin, *Adv. Funct. Mater.* **2025**, 2506057.
[74] A. J. Skarpeid, H. G. Hugdal, T. Salamone, M. Amundsen, S. H. Jacobsen, *J. Phys. Condens. Matter.* **2024**, *36*, 235302.

© 2025 The Author(s). Advanced Functional Materials published by Wiley-VCH GmbH

16163028, 2026, 4, Downloaded from https://advanced.onlinelibrary.wiley.com/doi/10.1002/adfm.202515722 by Universidad Complutense De Madrid, Wiley Online Library on [16/02/2026]. See the Terms and Conditions (https://onlinelibrary.wiley.com/terms-and-conditions) on Wiley Online Library for rules of use; OA articles are governed by the applicable Creative Commons License

[75] E. Mengotti, L. J. Heyderman, A. F. Rodríguez, F. Nolting, R. V. Hügli, H.-B. Braun, *Nat. Phys.* **2011**, *7*, 68.
[76] A. May, M. Saccone, A. van den Berg, J. Askey, M. Hunt, S. Ladak, *Nat. Commun.* **2021**, *12*, 3217.
[77] L. Berchialla, G. M. Macauley, L. J. Heyderman, *Appl. Phys. Lett.* **2024**, *125*, 22.
[78] L. Aballe, M. Foerster, E. Pellegrin, J. Nicolas, S. Ferrer, *J. Synchrotron Radiat.* **2015**, *22*, 745.
[79] M. Zajac, T. Giela, K. Freindl, K. Kollbek, J. Korecki, E. Madej, K. Pitala, A. Kozioł-Rachwał, M. Sikora, N. Spiridis, et al., *Nucl. Instrum. Methods Phys. Res. B* **2021**, *492*, 43.
[80] J. Szlachetko, J. Szade, E. Beyer, W. Błachucki, P. Ciochoń, P. Dumas, K. Freindl, G. Gazdowicz, S. Glatt, K. Guła, et al., *Eur. Phys. J. Plus* **2023**, *138*, 1.
[81] M. Foerster, J. Prat, V. Massana, N. Gonzalez, A. Fontsere, B. Molas, O. Matilla, E. Pellegrin, L. Aballe, *Ultramicroscopy* **2016**, *171*, 63.

© 2025 The Author(s). Advanced Functional Materials published by Wiley-VCH GmbH

16163028, 2026, 4, Downloaded from https://advanced.onlinelibrary.wiley.com/doi/10.1002/adfm.202515722 by Universidad Complutense De Madrid, Wiley Online Library on [16/02/2026]. See the Terms and Conditions (https://onlinelibrary.wiley.com/terms-and-conditions) on Wiley Online Library for rules of use; OA articles are governed by the applicable Creative Commons License